Proceedings of the 15th International Symposium on Unsteady Aerodynamics, Aeroacoustics & Aeroelasticity of Turbomachines
ISUAAAT15
24-27 September 2018, University of Oxford, UK

ISUAAAT15-065

TIME DOMAIN FLUTTER SIMULATIONS OF A STEAM TURBINE STAGE USING SPECTRAL 2D NON-REFLECTING BOUNDARY CONDITIONS

Daniel Schlüß*
German Aerospace Center (DLR)
Institute of Propulsion Technology
Cologne, Germany

Christian Frey
German Aerospace Center (DLR)
Institute of Propulsion Technology
Cologne, Germany

ABSTRACT

In this paper, we show the application of spectral two-dimensional non-reflecting boundary conditions (NRBC) in unsteady time domain simulations of three-dimensional turbomachinery flows. For this purpose, we conduct flutter simulations of a steam turbine stage and study the impact of the boundary condition formulation as well as of the boundary location on the prediction of aeroelastic properties. The main outcome is that spectral NRBC can be applied in challenging time domain simulations of realistic unsteady turbomachinery flows. Their reflection properties are shown to be superior to characeristic one-dimensional NRBC which significantly improves the prediction of aeroelastic quantities. In contrast to a prior implementation of spectral NRBC by the authors, convergence issues or a massive increase in computational costs, which would restrict the practical applicabilty of the spectral NRBC, do not occur.

INTRODUCTION

Spurious, numerical reflections from artificial inflow and outflow boundaries can strongly affect results of unsteady turbomachinery flow simulations. This is in particular detrimental when studying flow phenomena related to relatively small pressure perturbations, such as flutter or noise. Turbomachinery flows are characterised by periodically unsteady flow phenomena. Therefore, linear (c.f. e.g. [1, 2]) and non-linear (c.f. e.g. [3, 4]) frequency domain methods have become popular to efficiently study unsteady turbomachienry flows. Spectral boundary conditions are widely used in frequency domain flow solvers to overcome such reflections (e.g. [5–8]).

Since these boundary conditions are formulated non-locally in time, their implementation and application in time domain simulations is not straightforward. Yet, it appears highly beneficial to have such NRBCs also available for time-marching methods. Time domain simulations are the method of choice when phenomena are considered that either are not related to a specific frequency or the corresponding frequency is not known precisely, e.g. transient flows or vortex shedding and other boundary layer instabilities. Secondly, extensive experience with frequency domain methods is required before these methods will perhaps replace widely acknowledged time domain simulations. Thus, there is a need for accurate and consistent boundary conditions in time domain solvers to generate validation data.

Chassaing and Gerolymos [9] present a time domain implementation of spectral boundary conditions and demonstrate their good reflection properties for single acoustic modes in uniform mean flow. However, they observe slow convergence and their test case is rather basic. We have observed similar issues with a straightforward adoption of the spectral NRBC from our harmonic balance solver [10]. This implementation yielded good reflection properties, but its applicability was limited.

We have reimplemented two-dimensional spectral non-reflecting boundary conditions in DLR's solver for turbomachinery flows TRACE. Our implementation considers some time domain specific aspects which substantially improves robustness and convergence. Moreover, the reworked implementation does not constrain the domain decompositioning of the flow solver as we incorporate the necessary communication routines to account for the non-local nature of spectral NRBC. We apply the boundary conditions to a demanding turbomachinery test case, viz. the analysis of flutter in the last stage of a steam turbine.

*Address all correspondence to this author.

NOMENCLATURE

A	Area
a	Speed of sound
b_R	Rotor blade span
c	One-dimensional characeristics
$c_{R,m}$	Rotor chord length at midspan
d	Surface displacement
i	Complex unit
I	Identity matrix
k	Harmonic index (subscript)
k	Boundary-normal wavenumber
l	Circumferential wavenumber
L,R	Left- and right eigenvector matrix
L_{1D},R_{1D}	One-dimensional case ($l = 0$) of L and R
m	Non-dimensional circumferential wavenumber, equivalent to nodal diameter ($m = lr$)
M	Modal mass
n	Time step (superscript)
N	Number of time steps per period
p	Pressure
$p_{dyn,R,in}$	Mean dynamic pressure ($p_t - p$) at rotor inlet
q	Vector of primitive flow variables
r_i	i-th eigenvector within spectral analysis
r	Radius
t	Time
t	Stagnation quantity (subscript)
u,v,w	Velocity components
V_{Exit}	Velocity magnitude at rotor exit
W_{aero}	Aerodynamic work per cycle
Re	Real part of a complex quantity (also as subscript)
Im	Imaginary part of a complex quantity (also as subscript)
γ	Heat capacity ratio
ρ	Density
σ	Interblade phase angle
Ω	Rotational speed
ω	Angular frequency
ω^*	Reduced frequency
$\hat{x}$	Fourier coefficient of x
$\overline{x}$	Mean of x
$x^{in,out}$	Supersripts denoting incoming and outgoing components of vectors or matrices x
IBPA	Interblade phase angle
LPT	Low pressure turbine
NRBC	Non-reflecting boundary condition
(U)RANS	(Unsteady) Reynolds-averaged Navier-Stokes

SPECTRAL NRBC

In this section, we will briefly outline the concept of spectral non-reflecting boundary conditions. For a more detailed description, the reader is referred to e.g. [10, 11]. We will also address some important aspects related to the implementation of such boundary conditions for unsteady, time domain simulations. However, the focus of this work is on the application of the spectral NRBC in time domain simulations of a demanding test case. Therefore, we intend to publish a more elaborate description of time domain related implementation details in a later work.

The pivotal concept of the spectral NRBC is to decompose the unsteady flow field into incoming and outgoing modes and suppress the incoming ones. Disregarding changes in radial direction and viscous effects, the spectral NRBC in this paper are derived assuming two-dimensional Euler flow with sufficiently small perturbations in a stream-surface. Hence, we consider the linearised two-dimensional Euler equations:

$$\frac{\partial q}{\partial t} + A\frac{\partial q}{\partial x} + B\frac{\partial q}{\partial y} = 0 \tag{1}$$

Note that within the theory section, x and y denote the axis normal to the boundary and along the boundary in circumferential direction. The same holds for the corresponding velocity components u and v while the radial velocity component is given by w. For the full matrices and vectors in this section, the reader is referred to the appendix. In the context of the linearised two-dimensional Euler equations, any flow field can be described by superposition of wave-like perturbations

$$q = \mathrm{Re}\left(\hat{q}_{(\omega,l)}\, e^{\mathrm{i}(kx+ly+\omega t)}\right) \tag{2}$$

around an underlying mean flow $\overline{q}$. In the following, we will develop a modal transform for any perturbation with distinct angular frequency ω and pitch-wise wavenumber l yielding modal amplitudes with known directions of propagation. For this purpose, the dispersion relation is obtained by substituting (2) in the linearised Euler equations (1):

$$\det\left(\omega I + kA + lB\right) = 0 \tag{3}$$

or equivalently

$$\det\left(\omega A^{-1} + kI + lA^{-1}B\right) = 0. \tag{4}$$

This equation is the characteristical polynomial to the eigenvalue problem with eigenvalues $-k$ and right eigenvectors r_i:

$$\left(\omega A^{-1} + lA^{-1}B\right) r_i = -k r_i. \tag{5}$$

The eigenvectors describe the variation of primitve variables by fundamental perturbations. A common approach is to choose the eigenvectors such that they correspond to an entropy ($i = 1$), an in-plane vorticity ($i = 2$), an out-of-plane vorticity ($i = 3$), an downstream ($i = 4$) and an upstream propagating acoustic ($i = 5$) perturbation. Their direction of propagation can be determined by means of equation (3). For flows that have subsonic velocity components normal to the boundary, the first four waves travel in mean flow

direction, i.e. they enter the domain at inflow boundaries whereas the upstream acoustic wave is an outgoing perturbation there, and vice versa at outflow boundaries. The transformation matrix L that decomposes $\hat{q}_{(\omega,l)}$ into these fundamental perturbations is given be the inverse of the right eigenvector matrix:

$$L_{(\omega,l)} = R^{-1}_{(\omega,l)} = (r_1\ r_2\ r_3\ r_4\ r_5)^{-1} \tag{6}$$

By allowing only outgoing perturbations and enforcing amplitudes of incoming perturbations to be zero, one attains non-reflecting behaviour of artificial boundaries. Thus, for any mode, i.e. any set of angular frequency and circumferential wavenumber, the condition for no incoming perturbations reads:

$$L^{in}_{(\omega,l)} \hat{q}_{(\omega,l)} = 0 \tag{7}$$

Note that the distinction of components related to incoming and outgoing perturbations has to be row-wise for the modal transformation matrix L and column-wise for the eigenvector matrix R.

We achieved a significant improvement in robustness compared to our prior implementation of spectral NRBC by expressing the above condition in terms of one-dimensional characteristics $c = L_{1D}\, q$. As one-dimensional perturbations, i.e. plane waves orthogonal to the boundary, are represented by modes with $l = 0$, the corresponding transformation does not depend on the circumferential wavenumber and it can be scaled such that it is also independent of the angular frequency. Thus, characteristics can be used to define a temporally and spatially local, and therefore rather simple, one-dimensional non-reflecting boundary condition:

$$c^{in} = L^{in}_{1D}\, q = 0 \tag{8}$$

As such boundary conditions are known to be rather robust, we formulate the spectral two-dimensional NRBC as a modification to the characteristic boundary condition. Instead of requiring $c^{in} = 0$, we determine target characteristics by means of the spectral approach. Decomposing $\hat{q}_{(\omega,l)}$ into contributions from upstream and downstream propagating characteristics, we rewrite equation (7):

$$L^{in}_{(\omega,l)} \hat{q}_{(\omega,l)} = L^{in} \left(R^{in}_{1D}\, \hat{c}^{in}_{(\omega,l),target} + R^{out}_{1D}\, \hat{c}^{out}_{(\omega,l)} \right) = 0 \tag{9}$$

We extrapolate $\hat{c}^{out}_{(\omega,l)}$ from the boundary adjacent cells and obtain:

$$\hat{c}^{in}_{target,(\omega,l)} = \left[- \left(L^{in}_{(\omega,l)} R^{in}_{1D} \right)^{-1} L^{in}_{(\omega,l)} R^{out}_{1D}\, \hat{c}^{out}_{(\omega,l)} \right] \tag{10}$$

Note that the mean incoming target characteristics $\hat{c}^{in}_{target,(0,0)}$ are not to be computed from the spectral theory.

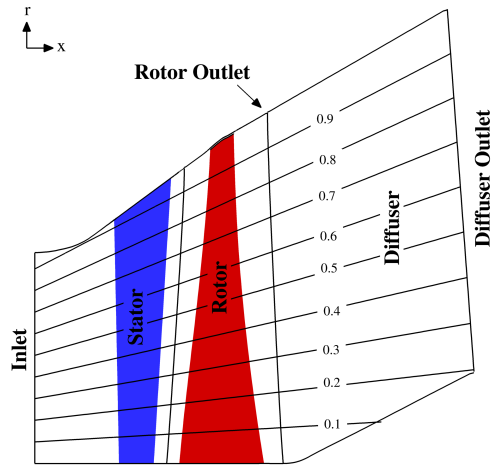

FIGURE 1: Schematic of the steam turbine stage depicting the computational domain and the definition of relative span.

Instead, they can be modified such that the average boundary flow state satisfies user-defined boundary values. Local incoming target characteristics can now be reconstructed by an inverse Fourier transform. If the face state is driven towards this target state with a suitable relaxation, the spectral NRBC appear to be comparable in terms of robustness to the one-dimensional boundary conditions.

The spectral approach applied to time-marching simulations requires the boundary flow field to be Fourier transformed in time and space, viz. along the boundary in pitchwise direction. Instead of storing the entire history of the boundary flow field, we determine the temporal Fourier coefficients in an iterative manner similar to harmonic store approach in phase lag methods (c.f. [12, 13]):

$$\hat{q}^n_k = \hat{q}^{n-1}_k + \frac{1}{N} \left(q^n - \tilde{q}^n \right) e^{-\mathrm{i}k\omega t} \tag{11}$$

Here, $\tilde{q}^n$ denotes the flow state at time step n reconstructed from the latest set Fourier coefficients. For all computations shown in this work, we consider ten temporal harmonics of the base frequency for the spectral boundary conditions.

APPLICATION

Steam Turbine Test Case

To assess the reflection properties, efficiency and stability of these boundary conditions in a real turbomachinery test case, we study flutter stability of a transonic three-dimensional steam turbine stage. The configuration has originally been established at Durham University [14] and later been proposed as open, numerical test case for flutter of steam turbines by the KTH turbomachinery group. The geometry, the mode shape and further information on the flutter configuration can be found in [15] and on the corresponding website [16]. We will compare our results to references [17] obtained by means of the time-linearised

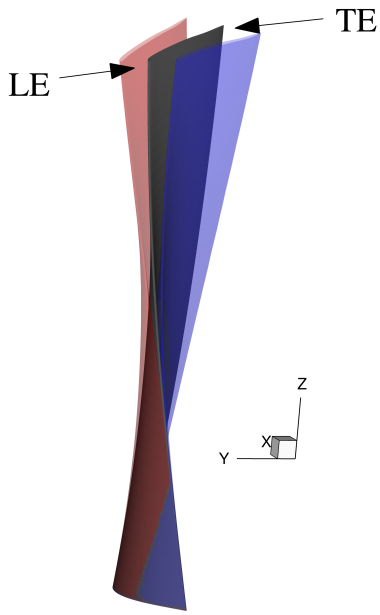

FIGURE 2: Illustration of bending mode magnified by a factor of twenty.

flow solver LUFT, which utilises three-dimensional NRBC (c.f [18]), and the commercial non-linear time domain solver CFX.

TABLE 1: Overview of operating conditions and other parameters for non-dimensionalisation.

$p_{t,Inlet}$	27	kPa
$T_{t,Inlet}$	340	K
p_{Outlet}	8.8	kPa
Ω	3000	$\frac{1}{\text{min}}$
b_R	920	mm
$c_{R,m}$	163.2	mm

Figure 1 shows a sketch of the configuration consisting of a stator row with 60 blades, a rotor row with 65 blades and a downstream diffuser. We define a simplified, linear distribution of relative span according to [15, 16]. The operating conditions are taken from the same sources and summarized in Table 1. The inflow is roughly axial. In this study, we included the original tip gap (c.f. [14]) of 4.2 mm or about 0.5 % relative span. Sun et al. study the impact of the tip clearance [17]. However, they compare a downsized gap of 0.25 % relative span and a model without tip gap.

We study the first bending mode of the rotor. The normalised mode shape is provided on the KTH website [16]. We scale this mode such that the maximum displacement at the tip trailing edge is 3 mm, which is in the order of the trailing edge thickness. The bending mode magnified by

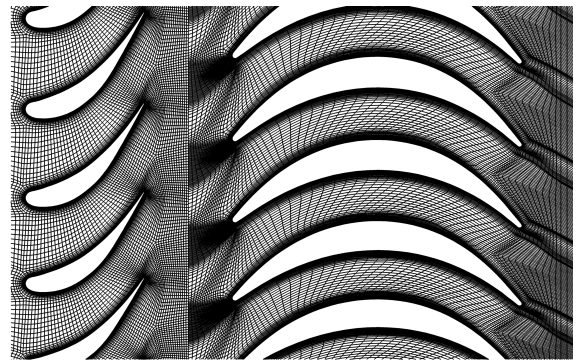

(a) Hub

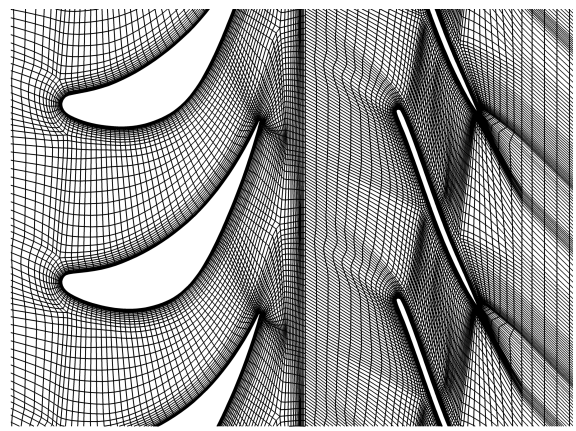

(b) Shroud

FIGURE 3: Details of mesh coarsened by factor 2 and duplicated in periodic direction.

a factor of twenty is depicted in Figure 2. We adopt the modified modal frequency of 132.08 Hz from [16], which is equivalent to a reduced frequency of $\omega^* = \frac{\omega\, c_{R,m}}{V_{Exit}} = 0.3$.

Numerical Setup

TABLE 2: Ideal gas parameters used for the steam turbine.

R	461.52	$\text{J}\cdot\text{kg}^{-1}\cdot\text{K}^{-1}$
γ	1.12	-
μ	$1.032\cdot10^{-5}$	$\text{N}\cdot\text{s}\cdot\text{m}^{-2}$

We employ the presented two-dimensional spectral NRBC in time-marching URANS flutter simulations of the rotor using DLR's flow solver TRACE (c.f. [19]). The underlying mean flow is calculated in a steady simulation beforehand. Here, the exit pressure is imposed at midspan of the diffuser outlet along with a radial equilibrium condition. The diffuser domain is included in the rotor system without an additional interface. In order to assess the boundary conditions' reflection properties, we also conduct flutter simula-

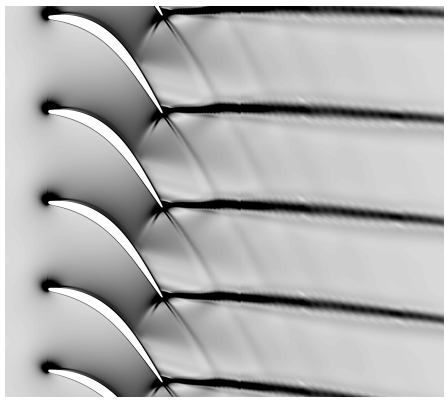

(a) 50 % span

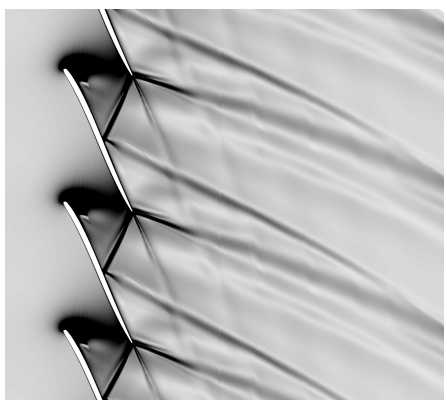

(b) 90 % span

FIGURE 4: Pseudo schlieren image of the flow in the rotor blade region at slices of constant relativ span.

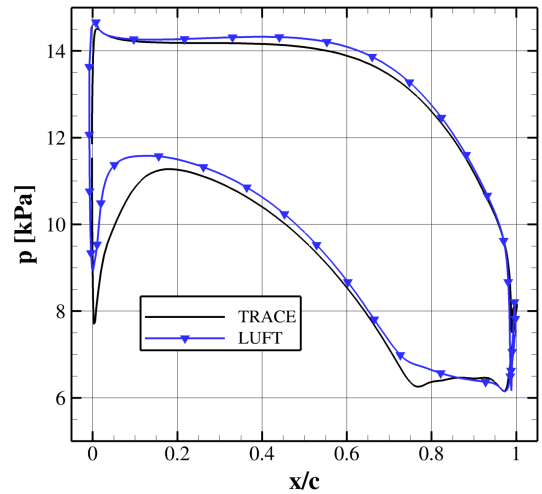

(a) 50 % span

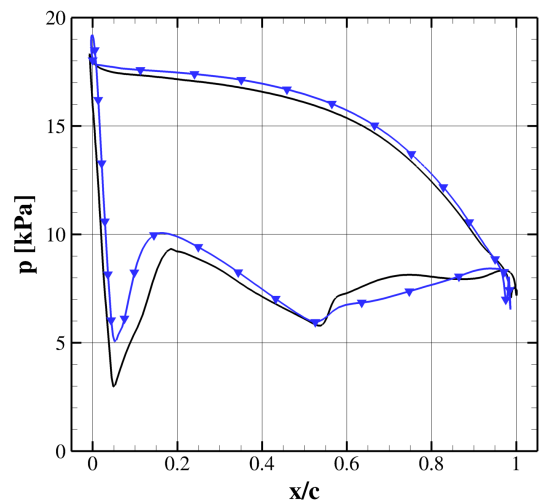

(b) 90 % span

FIGURE 5: Steady blade pressure distribution at two radial positions compared to references from [16].

tions on a shorter computational domain without the diffuser (see Figure 1) and computations using characteristic, one-dimensional boundary conditions as a reference. The short configuration is a demanding test case for the boundary condition as the oscillating trailing edge shock impinges on the outflow boundary. The circumferentially averaged pressure profile is extracted from the steady simulation at the rotor exit plane and the diffuser exit plane. These profiles are then prescribed in the unsteady simulation at their respective position. To ensure comparability between simulations using the long and the short domain, we checked that the massflow remains constant.

The computational mesh is generated by means of our inhouse tool PyMesh [20] and comprises about four million cells in total, about 2.1 million cells thereof in the rotor domain and another 0.7 million in the diffuser domain. Note that this is a finer resolution compared to the mesh used to obtain the reference results in [16, 17]. Blade wall boundary layers are resolved with $y^+ \approx 1$ whereas we employed wall functions at hub and casing walls with $30 < y^+ < 80$. Details of the mesh are depicted in Figure 3.

For all computations Wilcox's k-ω turbulence model [21] is used and ideal gas with constant molecular viscosity and the paramteres given in Table 2 is assumed. This assumption is justified for flutter simulations of the last steam turbine stage as shown by Petrie-Repar [22]. To conduct single passage simulations for arbitrary IBPAs, we use the phase lag method (c.f. [13,23]). We employ an implicit dual time stepping algorithm using the BDF2 scheme with 128 physical time steps per cycle and 50 pseudotime steps per physical time step. For IBPAs of -100°, -72°, -45°, 0°, 72° and 180°, simulations with both boundary condition types and both computational domains are carried out.

Steady Results

The mean flow in the rotor is characterised by a system of trailing edge shocks due to high exit Mach number compared to a typical gas turbine LPT. Figure 4 depicts this shock system by plotting the density gradient magnitude to mimic schlieren images of slices at 50 % and 90 % relative span. In particular at 90 % span, the pressure side branch of the trailing edge shock impinges on the neighbouring

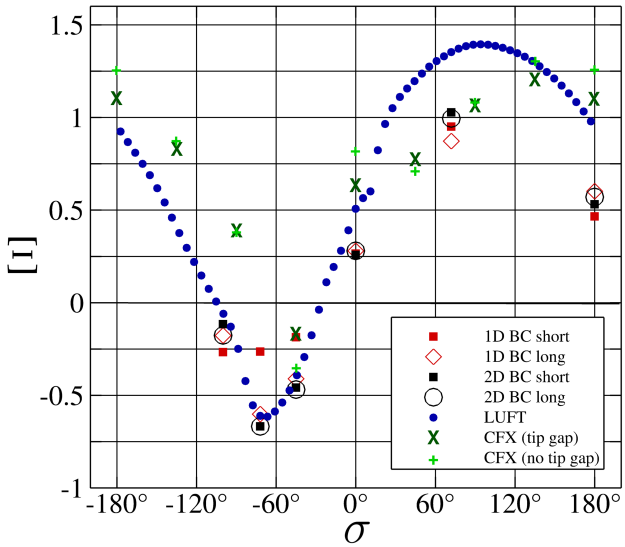

FIGURE 6: Non-dimensional aerodynamic damping versus IBPA.

blade's suction side at about 50 % chord length. Additionally, a strong expansion zone at the suction side's leading edge region, indicating a considerable incidence angle, can be observed at 90 % span.

These features also become evident in Figure 5. It plots the rotor blade pressure distribution at the same positions in comparison to results from [16] obtained with LUFT. Both solvers predict the steady blade pressure in good agreement. However, the leading edge suction peak and the subsequent shock are predicted stronger in the TRACE result. The same holds for the pressure rise at about half chord related to the incident shock. A possible explanation for these differences is the fact that the mesh used in this work comprises about twice as much cells in the rotor domain as the mesh used in the references. Nevertheless, we consider the steady flow solutions similar so that they pose a suitable basis for the following investigation of flutter. This is supported by the analysis of global performance quantities. TRACE predicts a mass flow of $\dot{m} = 85.43\,\mathrm{kg\,s^{-1}}$, a total-to-static isentropic efficiency $\eta_{ts} = 83.676\,\%$ and a power output of $P = 11.71\,\mathrm{MW}$. These values agree well with the results in [17] and [15] considering the larger tip gap in our setup.

Flutter analysis

Let us consider the non-dimensional damping

$$\Xi = \frac{-W_{aero}}{\pi\, b_R\, \alpha^2\, {c_{R,m}}^2\, p_{dyn,R,in}} \tag{12}$$

where $\alpha = d_{max}/c_{R,m}$ denotes the non-dimensionalised maximum displacement. The average dynamic pressure in the rotor inlet plane is $p_{dyn,R,in} = 2127.7\,\mathrm{Pa}$. Figure 6 plots the non-dimensional aerodynamic damping as a function of the IBPA for both types of boundary conditions and both domains. It also includes references from [17]. Recall that the

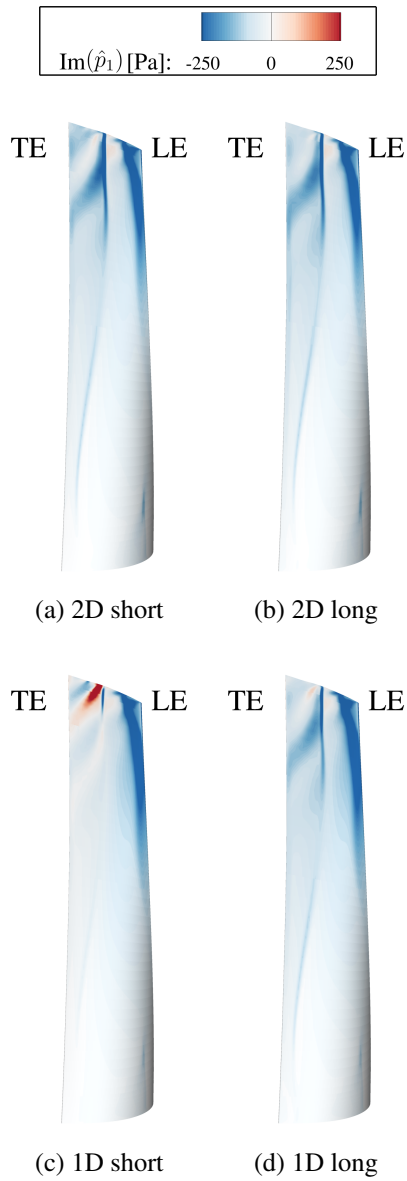

(a) 2D short (b) 2D long

(c) 1D short (d) 1D long

FIGURE 7: Distribution of unsteady pressure on rotor suction side associated to the fundamental harmonic (imaginary part).

tip gap in this source is about half as big as the one in our configuration.

In general, there is a good agreement between our results and the LUFT results. In particular, in the range of aerodynamic excitation, i.e. negative damping, the predicted damping values almost coincide when using spectral, two-dimensional NRBC or one-dimensional boundary conditions in the longer domain. The latter boundary conditions, however, lead to a significant deviation when employed together with the short domain.

The predicted damping values depend only to a small extend on the domain length in case of two-dimensional boundary conditions. As the position of the boundary plane is expected to have an impact on the unsteady pressure field if reflections occur, the above observation suggests that

there is only a small amount of reflection when employing two-dimensional boundary conditions. Since the divergent diffuser geometry may interact with the radiated pressure perturbations from the moving blade, solutions from the long and the short domain cannot be strictly compared. Moreover, the assumption of the flow being purely two-dimensional is not fulfilled. Still, the small differences between the results from both domains using two-dimensional boundary conditions indicate superior reflection properties of this boundary conditions to the one-dimensional ones.

Note that for the $\sigma = 0°$ case the one-dimensional boundary conditions produce almost the same damping values as the two-dimensional boundary conditions for both exit locations. This is due to the fact that, in this specific case of synchronously vibrating blades, plane waves arise that leave the domain orthogonally to the boundary and, hence, can also be absorbed by one-dimensional boundary conditions.

The CFX results display a weaker agreement with the other results, especially in the region in which TRACE and LUFT predict excitation. Yet, they serve to give an estimation of the influence of the tip gap consideration. This influence appears to be not very strong for most cases.

In the following, we will examine the $\sigma = -45°$ case in more detail. Figure 7 plots the imaginary part of the complex first harmonic pressure on the rotor suction side. As the imaginary part of the pressure, along with the associated structural mode, determines the aerodynamic work and damping, this figure reveals where the differences in global damping emerge. In the solution from the simulation using one-dimensional boundary conditions and the short mesh, the distinct line, where the oscillating shock from the neighbouring blade impinges, is diminished in comparison to all other solutions. Furthermore, in the tip region, a spot of high (imaginary) pressure can be discovered in the short 1D solution.

To compare this observation with the references, we introduce the local work coefficient

$$w = \frac{dW_{aero}/dA}{\pi\alpha^2 c_{R,m}\, p_{dyn,R,in}}. \tag{13}$$

Figure 8 shows the local work coefficient at 50 % and 90 % relative span. Several conclusions can be drawn from this figure: Firstly, our results, apart from the solution with the short domain and one-dimensional NRBC, agree qualitatively with the LUFT results at 90 % span. The largest differences occur close to the suction side's leading and trailing edge. In their tip gap study [17], Sun et al. find out that including the tip gap causes the front peak to be flattened. Hence, the smaller work coefficient of our computations in the leading edge region possibly results from the larger tip gap model. The larger peak in our simulations at 55 % chord length, where the neighbouring blade's trailing edge shock hits the suction side, is related to the observation in the steady results, that the pressure rise due to the impinging shock is predicted stronger in our results. This, again, is possibly related to the finer mesh used in this work. The solution with the short domain and one-dimensional NRBC,

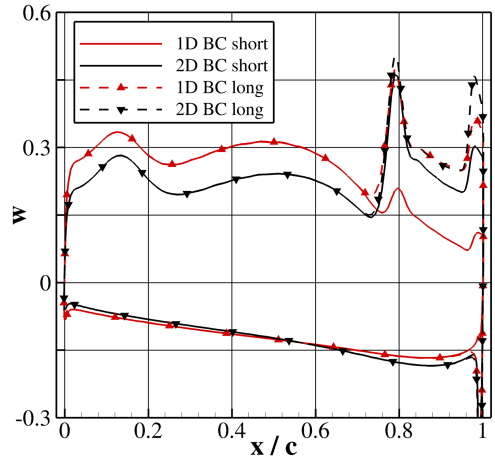

(a) 50 % span

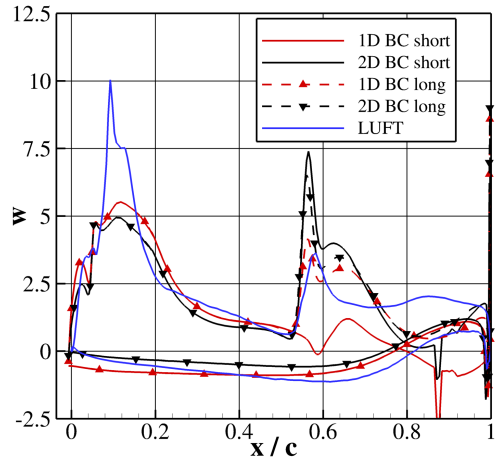

(b) 90 % span

FIGURE 8: Local work coefficients at two radial positions compared to references from [16].

however, deviates especially in this region from the other TRACE results.

Moreover, the work coefficient distributions at both radial positions reveal that the solution upstream of the shock impingement position is independend of the exit position and hence not affected by possible reflections from the outlet. However, in the front region, the work coefficient varies with the inflow boundary method, yet to a smaller extend. Note that the rotor inlet position is constant for all simulations. Thus, the solutions obtained with the long and the short domains coincide in the front region.

In the following, we will study the dominant mode associated to the blade motion, i.e. the pressure perturbation with non-dimensional circumferential wavenumber $m = -8.125$ at the blade vibration frequency. Figure 9a plots the pressure amplitude of this wave depending on the radial positon. This mode can be decomposed into fundamental waves by means of the wave splitting approach used for the spectral NRBC. The contribution of the incoming downstream propagating acoustic mode is depicted in Figure 9b. As expected, the amplitude of the incoming acoustic mode is equal to zero

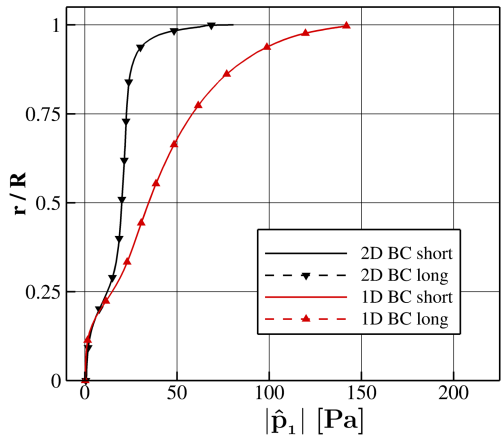

(a) full amplitude

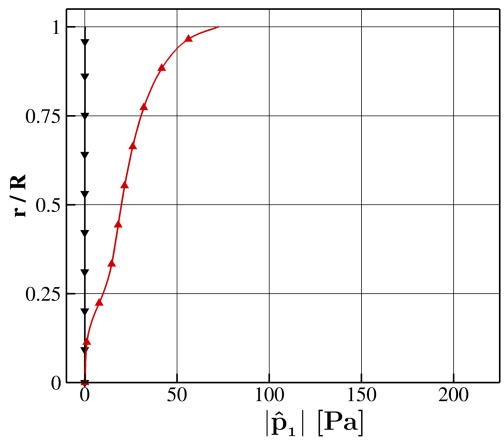

(b) downstream acoustic wave

FIGURE 9: Pressure amplitude of the dominant mode ($k = 1, m = -8.125$) versus span at rotor inlet.

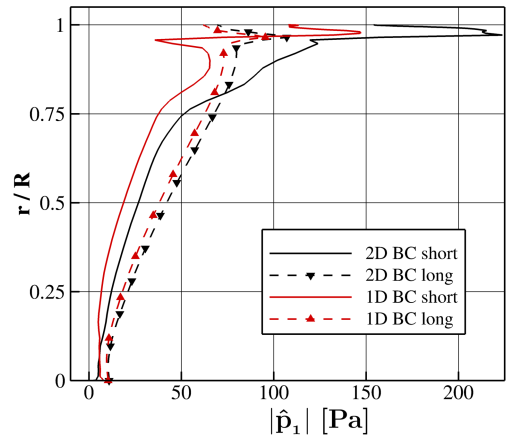

(a) full amplitude

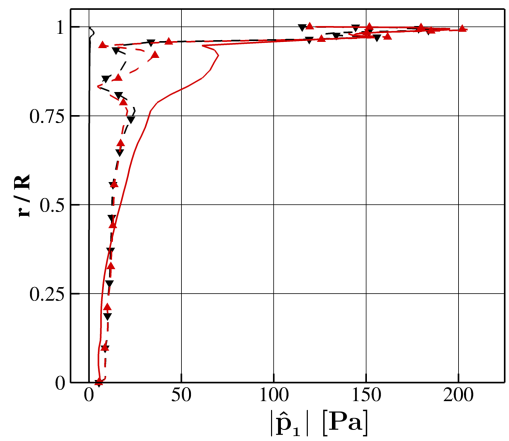

(b) upstream acoustic wave

FIGURE 10: Pressure amplitude of the dominant mode ($k = 1, m = -8.125$) versus span at rotor outlet.

when using the spectral boundary conditions. The discrepancy between the one-dimensional and the two-dimensional solution in Figure 9a is consistent with the amplitude of the incoming acoustic mode when using one-dimensional NRBC. This indicates that the differences of the local work coefficient in the front region can be attributed to reflections from the inlet boundary. Of course, the analysis based on a two-dimensional linearised Euler approach can only serve to give a certain estimation, but not a quantitatively precise evaluation of the real upstream and downstream propagating modes.

The same analysis is performed at the rotor outlet plane and shown in Figure 10. Both the long and the short mesh results are evaluated at the short rotor outlet plane. The analysis yields findings similar to the inlet. Furthermore, it shows the impact of the outlet boundary position. There is a considerably stronger incoming wave in the outer 25 % span region when one-dimensional NRBC are applied on the short mesh. Additionally, one observes that the tip leakage vortex produces strong perturbations close to the casing. Such perturbations cannot be correctly accounted for by both methods. Figure 10b exhibits a relatively weak, but significant incoming wave for the long domain simulations. As its amplitude is approximately constant over the whole span, it is supposed that this mode does not stem directly from the blade motion, which, in contrast, is approximately proportional to the relative spanwise position. Further investigation is needed to clarify which of the following possible reasons is responsible for this observation. Firstly, the circumferential Fourier decomposition is not corrected for the residual grid motion at the short rotor outlet as the imposed grid motion decays from the blade to the actual outlet boundary at the diffuser exit. So this might be a pure postprocessing artefact. Another possible explanation is that there is a true three-dimensional interaction of the diffusor geometry with the acoustic mode radiated downstream from the blade. Beyond, the upstream wave could be an artificial reflection from the outlet boundary as the prerequisites of the boundary condition theory might be violated. However, the one-dimensional and the two-dimensional NRBC produce consistent incoming perturbations which seems unlikely considering the elementary differences of both methods.

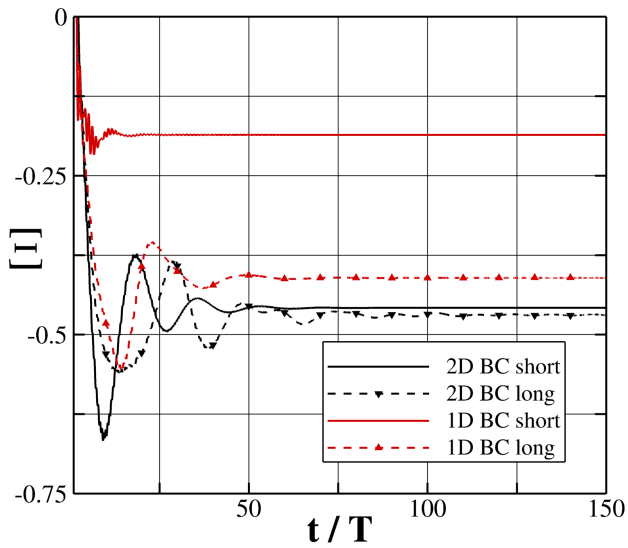

FIGURE 11: Temporal development of integral damping ($\sigma = -45°$).

Convergence and computational costs

Figure 11 plots the temporal development of integral damping over time. The spectral NRBC need about twice as many time steps to converge as the one-dimensional boundary conditions. This is due to the fact, that the spectral NRBC depend on the temporal Fourier coefficients of the boundary solution, which themselves converge rather slowly in phase lag simulations. However, there are no stability issues related to the boundary conditions in this study. The authors have experience with less satisfactory convergence characteristics of a prior implementation of spectral boundary conditions in time domain simulations. Therefore, this is a substantial improvement.

Furthermore, the reduced reflections of spectral NRBC allow shorter domains. The possibilty to use shorter domains, in turn, reduces the number of time steps required for convergence as one can infer from Figure 11. In this case, the spectral NRBC applied on the short domain and the one-dimensional NRBC along with the long domain take roughly the same number of time steps to reach convergence. Note that the long mesh comprises more cells and, hence, demands more computational resources if the run time is to be kept constant. On the other hand, the more complex spectral NRBC enlarge the computational effort of the boundary treatment. However, throughout all computations carried out in this work, the run time per time step of simulations using spectral NRBC is increased by only 0.5-1.5 % compared to the computations with one-dimensional boundary conditions while all other parameters are kept constant. Therfore, there is no clear answer to the question which boundary method is favourable if solely the computational effort is considered. Altogether, the computational costs of unsteady time domain simulations using spectral boundary conditons remain comparable to the costs of simulations using characteristic boundary conditions.

CONCLUSIONS AND OUTLOOK

We demonstrate the applicability of spectral, two-dimensional non-reflecting boundary conditions in time domain flutter simulations of a three-dimensional steam turbine configuration. The advantageous reflection properties of these NRBC are highlighted. Moreover, the necessity of using proper non-reflecting boundary conditions for certain investigations becomes evident from our results. The poor reflection properties of one-dimensional boundary conditions will lead to larger errors when it is not possible to consider a downstream diffuser in the computational domain, e.g. when one studies flutter of blades rows from multistage configurations.

For the presented test case, the robustness of the spectral NRBC is comparable to the robustness of characteristic boundary conditions. The run time of computations using the spectral NRBC is about one percent larger compared to the computations using characteristic boundary conditions. But more time steps are needed to obtain convergence. In contrast, the use of spectral boundary conditions allows shorter domains thanks to reduced artificial reflections which generally accelerates convergence.

For the future, a more detailed comparison between frequency domain solvers, like e.g. time-linearised or harmonic balance solvers, on the one hand and time domain solvers on the other hand is possible since inconsistencies from the boundary conditions have been eliminated. Another interesting application of the time domain solver in combination with the spectral NRBC is the investigation of non-linear effects in the aeroelastics of turbomachinery.

ACKNOWLEGDEMENTS

The authors would like to thank MTU Aero Engines for their support and co-sponsorship of the first author.

REFERENCES

[1] Verdon, M. D., and Montgomery, J. M., 1997. A three-dimensional linearized Euler analysis for turbomachinery blade rows unsteady. Tech. Rep. NASA Contractor Report 4770, United Technologies Research Center East Hartford, Connecticut.

[2] Kersken, H.-P., Frey, C., Voigt, C., and Ashcroft, G., 2012. "Time-linearized and time-accurate 3D RANS methods for aeroelastic analysis in turbomachinery". *Journal of Turbomachinery,* ***134***(5), p. 051024.

[3] He, L., 2010. "Fourier methods for turbomachinery applications". *Prog. Aerosp. Sci.,* ***46***(8), Nov., pp. 329–341.

[4] Hall, K. C., Thomas, J. P., and Clark, W. S., 2002. "Computation of unsteady nonlinear flows in cascades using a harmonic balance technique". *AIAA J.,* ***40***(5), May, pp. 879–886.

[5] Montgomery, M. D., and Verdon, J. M., 1997. A three-dimensional linearized unsteady euler analysis for turbomachinery blade rows. Tech. Rep. NASA CR-4770,

United Technologies Research Center, East Hartford, Connecticut, USA.

[6] Moinier, P., Giles, M. B., and Coupland, J., 2007. "Three-dimensional nonreflecting boundary conditions for swirling flow in turbomachinery". *J. Propul. Power,* ***23***(5), pp. 981–986.

[7] Petrie-Repar, P. J., McGhee, A. M., and Jacobs, P. A., 2007. "Three-dimensional viscous flutter analysis of standard configuration 10". In Proceedings of the ASME Turbo Expo 2007.

[8] Kersken, H.-P., Ashcroft, G., Frey, C., Wolfrum, N., and Korte, D., 2014. "Nonreflecting boundary conditions for aeroelastic analysis in time and frequency domain 3D RANS solvers". In Proceedings of ASME Turbo Expo 2014.

[9] Chassaing, J., and Gerolymos, G., 2007. "Time-domain implementation of nonreflecting boundary-conditions for the nonlinear euler equations". *Applied mathematical modelling,* ***31***(10), pp. 2172–2188.

[10] Schlüß, D., Frey, C., and Ashcroft, G., 2016. "Consistent non-refleflecting boundary conditions for both steady and unsteady flow simulations in turbomachinery applictations". In VII European Congress on Computational Methods in Applied Sciences and Engineering (ECCOMAS Congress 2016), M. Papadrakakis, V. Papadopoulos, G. Stefanou, and V. Plevris, eds.

[11] Giles, M. B., 1988. Non-reflecting boundary conditions for the Euler equations. Tech. rep., MIT Dept. of Aero. and Astr. CFDL Report 88-1.

[12] Gerolymos, G. A., and Chapin, V., 1991. "Generalized expression of chorochronic periodicity in turbomachinery blade-row interaction". *La Recherche Aérospatiale*(5), pp. 69–73.

[13] He, L., 1992. "Method of simulating unsteady turbomachinery flows with multiple perturbations". *AIAA J.,* ***30***(11), Nov., pp. 2730–2735.

[14] Burton, Z., 2014. "Analysis of low pressure steam turbine diffuser and exhaust hood systems". PhD thesis, Durham University.

[15] Qi, D., Petrie-Repar, P., Gezork, T., and Sun, T., 2017. "Establishment of an open 3d steam turbine flutter test case". In Proceedings of 12th European Conference on Turbomachinery Fluid dynamics & Thermodynamics.

[16] Department of Energy Technology, KTH Royal Institute of Technology, Stockholm, Sweden, 2018. 3D Steam Turbine Flutter Test Case. https://www.kth.se/en/itm/inst/energiteknik/forskning/kraft-varme/ekv-researchgroups/turbomachinery-group/aeromech-test-cases/3d-steam-turbine-flutter-test-case-1.706654. Online; Accessed on 18-08-2018.

[17] Sun, T., Petrie-Repar, P., and Qi, D., 2017. "Investigation of tip clearance flow effects on an open 3d steam turbine flutter test case". In ASME TurboExpo 2017, no. 50954, pp. V008T29A024–.

[18] Petrie-Repar, P. J., 2010. "Three-dimensional non-reflecting boundary condition for linearized flow solvers". In Proceedings of the ASME Turbo Expo 2010: Power for Land, Sea, and Air, American Society of Mechanical Engineers, pp. 1247–1252.

[19] Becker, K., Heitkamp, K., and Kügeler, E., 2010. "Recent progress in a hybrid-grid cfd solver for turbomachinery flows". In Proceedings Fifth European Conference on Computational Fluid Dynamics ECCOMAS CFD 2010.

[20] Weber, A., and Sauer, M., 2016. Pymesh - template documentation. Technical report DLR-IB-AT-KP-2016-34, German Aerospace Center (DLR), Institute of Propulsion Technology, Linder Hoehe, Cologne, Germany, February.

[21] Wilcox, D. C., 1988. "Reassessment of the scale-determining equation for advanced turbulence models". *AIAA J.,* ***26***(11), Nov., pp. 1299–1310.

[22] Petrie-Repar, P., Makhnov, V., Shabrov, N., Smirnov, E., Galaev, S., and Eliseev, K., 2014. "Advanced flutter analysis of a long shrouded steam turbine blade". In Proceedings of the ASME Turbo Expo 2014: Turbine Technical Conference and Exposition, American Society of Mechanical Engineers, pp. V07BT35A022–V07BT35A022.

[23] Schnell, R., and Nürnberger, D., 2004. "Investigation of the tonal acoustic field of a transonic fanstage by time-domain CFD-calculation with arbitrary blade counts". In ASME-Paper.

[24] Frey, C., and Kersken, H.-P., 2016. "On the regularisation of non-reflecting boundary conditions near acoustic resonance". In ECCOMAS Congress 2016 VII European Congress on Computational Methods in Applied Sciences and Engineering, Crete Island, Greece.

ANNEX: VECTORS AND MATRICES OF THEORY SECTION

The flux Jacobians of the 2D linearised Euler equations with respect to primitive variables and the vector of primitive variables read:

$$A=\begin{pmatrix}\overline{u} & \overline{\rho} & 0 & 0 & 0\\ 0 & \overline{u} & 0 & 0 & 1/\overline{\rho}\\ 0 & 0 & \overline{u} & 0 & 0\\ 0 & 0 & 0 & \overline{u} & 0\\ 0 & \gamma\overline{p} & 0 & 0 & \overline{u}\end{pmatrix}, B=\begin{pmatrix}\overline{v} & 0 & \overline{\rho} & 0 & 0\\ 0 & \overline{v} & 0 & 0 & 0\\ 0 & 0 & \overline{v} & 0 & 1/\overline{\rho}\\ 0 & 0 & 0 & \overline{v} & 0\\ 0 & 0 & \gamma\overline{p} & 0 & \overline{v}\end{pmatrix}, q=\begin{pmatrix}\rho\\ u\\ v\\ w\\ p\end{pmatrix}$$

The forward and backward characterics transformation matrices are given by:

$$L_{1D}=\begin{pmatrix}\frac{-1}{\overline{\rho}} & 0 & 0 & 0 & \frac{1}{\overline{\rho}\,\overline{a}^2}\\ 0 & 0 & \frac{1}{\overline{a}} & 0 & 0\\ 0 & 0 & 0 & \frac{1}{\overline{a}} & 0\\ 0 & \frac{1}{a} & 0 & 0 & \frac{1}{\overline{\rho}\,\overline{a}^2}\\ 0 & -\frac{1}{a} & 0 & 0 & \frac{1}{\overline{\rho}\,\overline{a}^2}\end{pmatrix}, \quad R_{1D}=\begin{pmatrix}-\overline{\rho} & 0 & 0 & \frac{\overline{\rho}}{2} & \frac{\overline{\rho}}{2}\\ 0 & 0 & 0 & \frac{\overline{a}}{2} & -\frac{\overline{a}}{2}\\ 0 & \overline{a} & 0 & 0 & 0\\ 0 & 0 & \overline{a} & 0 & 0\\ 0 & 0 & 0 & \frac{\overline{\rho}\,\overline{a}^2}{2} & \frac{\overline{\rho}\,\overline{a}^2}{2}\end{pmatrix}$$

The eigenvectors of the convective modes, i.e. entropy (r_1), in-plane vorticity (r_2) and out-of-plane vorticity (r_3)

read:

$$r_1 = \begin{pmatrix} -\overline{\rho} \\ 0 \\ 0 \\ 0 \\ 0 \end{pmatrix}, \quad r_2 = \begin{pmatrix} 0 \\ \overline{a}m \\ \frac{\overline{a}}{\overline{u}}(\omega r + mv) \\ 0 \\ 0 \end{pmatrix}, \quad r_3 = \begin{pmatrix} 0 \\ 0 \\ 0 \\ \overline{a} \\ 0 \end{pmatrix}$$

The acoustic modes are

$$r_{4,5} = \begin{pmatrix} \overline{\rho} \\ \overline{a}\frac{k_{4,5}}{\|\xi\|} \\ \overline{a}\frac{l}{\|\xi\|} \\ 0 \\ \gamma p \end{pmatrix}$$

with the $\xi = \begin{pmatrix} k \\ l \end{pmatrix}$ being the wavenumber vector in the underlying streamsurface. The boundary-normal wave numbers $k_{4,5}$ still have to be determined. With the three convective modes and their corresponding eigenvalues known, the characteristic polynomial (4) reduces to a quadratic equation, from which $k_{4,5}$ can be calculated:

$$(\omega + k_{4,5}\overline{u} + l\overline{v})^2 = \overline{a}^2\left(k_{4,5}^2 + l^2\right) \tag{14}$$

The reader is referred to [8, 11, 24] for further details including the final expressions for $k_{4,5}$ and $r_{4,5}$.

